Quantum beats in two-color photoionization to the spin-orbit split continuum of Ar

M. A. Alarcón[1], A. Plunkett[2], J. K. Wood[3], D. Biswas[2], C. H. Greene[1], and A. Sandhu[2,3,*]

[1]*Department of Physics and Astronomy, Purdue University, West Lafayette, Indiana 47907, USA*
[2]*Department of Physics, University of Arizona, Tucson, Arizona 85721, USA*
[3]*College of Optical Sciences, University of Arizona, Tucson, Arizona 85721, USA*

We report a study of the quantum beats in two-color photoionization of argon. An attosecond extreme ultraviolet pulse train prepares an electronic wave packet of definite odd parity, with total angular momentum $J = 1$, targeting the states between 14.0 and 14.5 eV from the ground state. Two-photon ionization of this wave packet with a tunable infrared probe pulse makes the constituent states interfere in both continuum channels, corresponding to the core angular momenta $j_c = 1/2$ and $3/2$, respectively. We analyze photoelectron spectrograms as a function of the time delay of the probe pulse and identify oscillations due to several pairs of states through Fourier decomposition. We observe phase differences between the corresponding beat signals in the two spin-orbit split continua. Comparison of theoretical simulations with the experimental measurements allows us to interpret the amplitudes and phases of ionization signals. We express the observed phase differences in terms of the off-diagonal elements of the short-range scattering matrix and the dipole matrix elements to the continuum eigenchannels.

I. INTRODUCTION

Time-resolved photoelectron interferometry has been proven to be an effective tool to measure the quantum beats of electronic wave packets in atoms [1–4] and molecules [5–7]. The energy dependence of beat signals in the continuum has been used to characterize the amplitudes and phases of ionization pathways in a variety of systems, involving multicolor ionization pathways, strong-field modification of the electronic structure, and correlated electron dynamics [8–15]. An interesting case arises when considering the ejection of the photoelectron into the spin-orbit split continua, which corresponds to the situation where ionization is accompanied by electronic rearrangement in one of the channels. Differential analysis of two spin-orbit split channels has led to interesting insights into photoemission delays [16], autoionization dynamics [17], and high-harmonic generation [18].

Our work is motivated by the desire to understand how short-range interactions between the outgoing electron and the ion core manifest in the phase of the quantum beats in two different continua. We apply this method to investigate a wave packet composed of the excited states of argon, as illustrated in Fig. 1(a). The argon ion features a spin-orbit splitting of 180 meV, with the ion's $j_c = 3/2$ ground state and the $j_c = 1/2$ excited state lying 15.76 eV and 15.94 above the neutral ground state, respectively [19]. A bound electronic wave packet can be prepared by exciting the system with an extreme ultraviolet (XUV) attosecond pump pulse train, followed by a two-photon ionization with a delayed infrared (IR) probe light pulse which makes the various components of the wave packet interfere in the two continua. The interference pattern can be resolved in kinetic energy, and its evolution exhibits quantum beating in the probe time delay with frequencies determined by pairs of constituent state energies. We observe that there is a phase difference between beating in the $j_c = 1/2$ and $3/2$ channels. We conduct a systematic experimental study and compare it with detailed theoretical calculations employing multichannel quantum-defect theory, involving an explicit propagation of the wave function, to understand the dependence of the phases on the various parameters of the probe light field. We find that the observed beating pattern reveals the complex resonant structure of the intermediate highly excited Rydberg states, which leads to a nontrivial dependence on the intensity and frequency of the probe. By analyzing the phase difference in the yield of electrons between ion thresholds and how it depends on fundamental atomic quantities, it is possible to probe indirectly off-diagonal elements of the scattering matrix describing the collisions of the electrons with the ion core in the close range as well as the dipole matrix elements to wave functions corresponding to the eigenstates of the scattering matrix.

II. EXPERIMENT

Our pump-probe scheme [Fig. 1(a)] involves an XUV pump pulse (14 eV) which excites an electronic wave packet in the neutral argon atom, followed by an IR probe pulse (1 eV) that ionizes the system after a variable time delay t_0. To generate the pump and probe pulses, a Ti:sapphire 780-nm laser amplifier with 2 mJ pulse energy, 40 fs, and linearly polarized pulse is split on a beam splitter into two arms. One arm is directed to an optical parametric amplifier (OPA) tuned for down-conversion to a 1200-nm probe pulse with
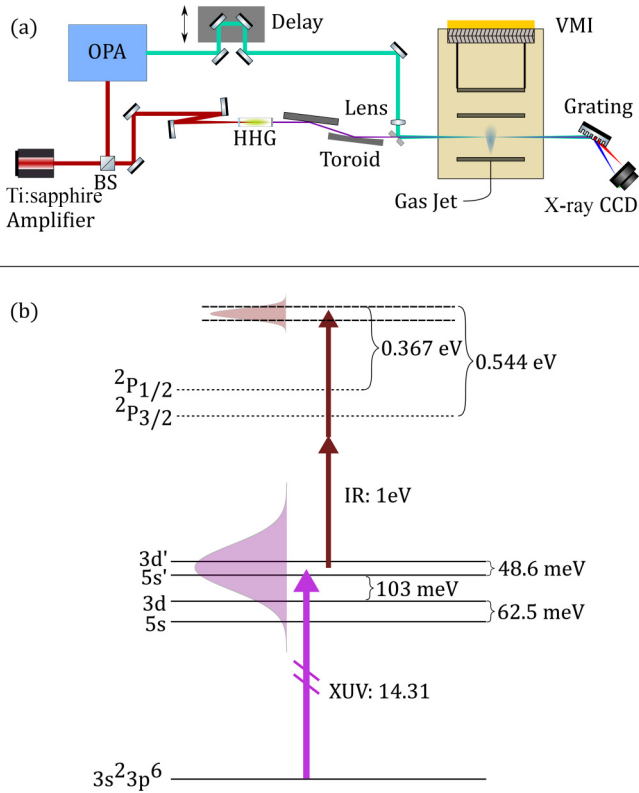
*asandhu@arizona.edu

FIG. 1. (a) Schematic of our experimental apparatus. A 40-fs, 2-mJ, 780-nm, linearly polarized beam is split into two arms. One arm generates a 1-eV probe pulse with controllable time delay while the other arm drives high harmonic generation in a Xe-filled gas cell generating an XUV pump pulse. The beams combine on a mirror with a hole and focus into an argon-effusive gas jet. (b) Energy levels relevant to our pump-probe experiment: The ninth harmonic of the XUV pump pulse prepares a wave packet encompassing both $(3d, 5s)$ and $(3d', 5s')$ pairs of states, which correspond to a Rydberg electron attached to the $j_c = 1/2$ and $3/2$ ion cores, respectively. After a time delay τ, the 1-eV probe pulse causes two-photon ionization of each state to the continua corresponding to both ion core thresholds. As an example, the expected kinetic energies of the $5s'$ and $3d'$ photoelectrons with respect to both spin-orbit split thresholds are listed.

approximately 65-fs pulse duration while the second arm is focused into a Xe gas cell for high harmonic generation. By tuning the spatial profile of the driving pulse, the pressure of Xe gas, and the location of the focus within the gas cell, we tune the phase-matching condition to produce odd harmonics 9–15 of the fundamental driving frequency, henceforth referred to as the XUV pump pulse. Using a toroidal mirror at grazing incidence, this XUV pulse is focused onto an effusive gas jet of argon emanating from a 75-μm hole in the repeller plate of a velocity map imaging (VMI) spectrometer inside the vacuum chamber. The probe pulse is focused to the same location using a 50-cm lens to reach an intensity of approximately 1 TW/cm^2 and made collinear with the XUV pulse using a flat mirror with a hole.

Figure 1(b) depicts an energy-level diagram relevant to our pump-probe scheme. Due to the large bandwidth, the ninth harmonic in the XUV pulse excites a wave packet composed

of $(^2P_{3/2})5s^2[3/2]_1^\circ$, $(^2P_{3/2})3d^2[3/2]_1^\circ$, $(^2P_{1/2})5s^2[1/2]_1^\circ$, and $(^2P_{1/2})3d^2[3/2]_1^\circ$ states. The term in parentheses indicates the ionic state, next is the orbital of the outermost electron, and the term in square brackets is the K quantum number corresponding to the eigenvalue associated with the square of the vector operator $\vec{K} = \vec{j_c} + \vec{\ell}$. The subindex at the end indicates total angular momentum and the upper index the parity. This notation is known as the jK notation. For brevity, and when the full spectroscopic notation is not essential, we will refer to the four aforementioned initial states as $5s$, $3d$, $5s'$, and $3d'$, respectively. The central energy of the ninth harmonic overlaps strongly with the $5s'$ and $3d'$ states; therefore, the relative amplitudes of the wave-packet constituents are not equal. The wave packet evolves for a time t_0, after which the IR probe pulse couples the wave packet to the continuum in the $j_c = 1/2$ and $3/2$ ion core channels via two-photon absorption. We collect the photoelectrons in a VMI spectrometer [10,20], and the resulting two-dimensional distribution is numerically Abel inverted using pBASEX to reconstruct the three-dimensional transverse photoelectron momentum distribution [21]. Angular integration produces electron yield as a function of photoelectron kinetic energy. The amplitude error bars in the experimental results stem from detector inhomogeneities, and they are estimated by subdividing the detector into quadrants. We used autoionizing lines of argon between the two spin-orbit split ionization thresholds to calibrate photoelectron energy and obtain energy error bars.

III. RESULTS

At each time delay we calculate the difference spectrum (XUV pump + IR probe) − (XUV pump). The difference spectra at each time delay are stitched together to create a difference spectrogram, as seen in Fig. 2(a), which shows the change in electron yield due to the probe pulse as a function of probe pulse time delay and continuum kinetic energy of the photoelectron. In our previous study in [22], the difference spectrum revealed the interruption of the autoionization process on the autoionizing wave packet created by the XUV; in this case, the subtraction is done solely to increase the signal-to-noise ratio, since the XUV only spectrogram has very little signal in a 600-meV-wide region between 0.2 and 0.8 eV. Therefore, choosing an ideal OPA setting, i.e., the IR probe wavelength, positions the photoionization signal in the middle of this region separating the signal of interest from other processes.

In Fig. 2(a) we observe strong quantum beat signals with two dominant features visible around the photoelectron kinetic energies of 0.37 and 0.55 eV. From Fig. 1(b) we can loosely associate these features with $3d'$ ionizing to the $j_c = 1/2$ and $3/2$ ion core channels, respectively. With the theoretical methods that we will describe in the next section, we obtain the calculated spectrogram in Fig. 2(b), which shows remarkable agreement with the experimental result in Fig. 2(a). Both show oscillations in time which, as we describe later, oscillate with a frequency corresponding to the $3d'$-$5s'$ energy separation. From now on, we denote the energy separation among the four initial states by using parentheses, i.e., the beating frequency is $(3d', 5s')$. Importantly, we note the phase difference between the beat signal at 0.37 and 0.55 eV,
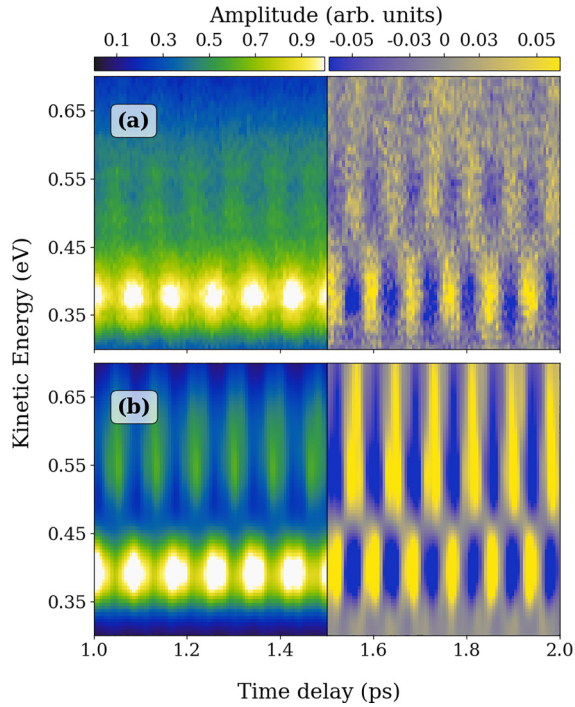
FIG. 2. (a) Photoelectron yield observed experimentally resolved in time delay. (b) Photoionization probability simulated by direct time propagation. Both (a) and (b) show strong quantum beats corresponding to the interference of the $3d'$ and $5s'$ states. The signal has been normalized by the maximum value of the time-delay average. To further highlight the beating, the time-averaged value has been subtracted from the signal, as shown for delays greater than 1.5 ps.
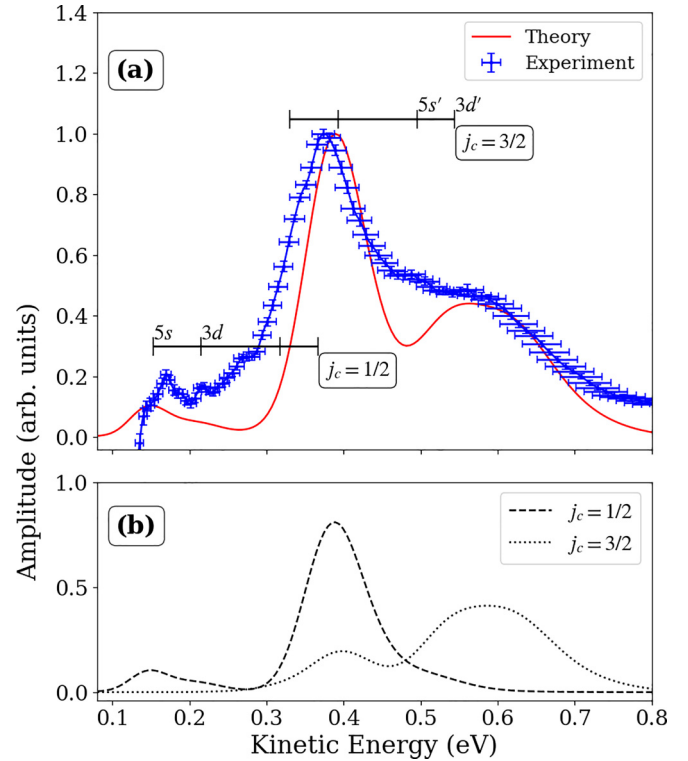

FIG. 3. (a) Time-delay-averaged photoelectron signal normalized to have unit maximum in both experiment (blue dashed line) and theory (red solid line). The horizontal lines and the ticks show the position of the expected energy from two-photon ionization from each $J = 1$ state. (b) Theoretical threshold resolved components of the ionization probability showing the signal dominated by $j_c = 1/2$ ionization of the $3d'$ and $5s'$ states.

making them almost out of phase; as we will explain in the coming section, this phase difference points to the role of short-range interaction between the outgoing electron and the ion core. Taking the average of the experimental and theoretical difference spectrograms in Figs. 2(a) and 2(b) along the time delay axis produces time-delay-averaged photoelectron spectra, as seen in Fig. 3(a). The vertical markers indicate the kinetic energy of photoelectrons from each of the constituent states relative to the $j_c = 1/2$ and $3/2$ ion states, as noted on the graph insets. The first two markers on each line refer to the $5s$ and $3d$ states, while the second two refer to the $5s'$ and $3d'$ states. Both experimental and theoretical spectra confirm the strong ionization signal from $3d'$ and $5s'$ states. To separately identify the contributions from each ionization channel, we obtained the dotted and dashed spectral curves in Fig. 3(b), which are calculated time-delay-integrated photoelectron spectra to the $j_c = 3/2$ and $1/2$ cores, respectively. These plots again confirm the strong contributions from the $3d'$ and $5s'$ states in both core channels.

To make the oscillatory signal more evident in Fig. 2 we have split the time-delay axis in two. For delays less than 1.5 ps, in both theory and experiment, we show the absolute photoionization measurement normalized to the maximum time-delay-averaged value. This highlights the two different ionization channels at distinct kinetic energies and shows the dominance of the $j_c = 1/2$ channel observed in both experiment and theory, as we will discuss below. For delays greater than 1.5 ps we subtract the time-delay-averaged signal

for every kinetic energy and so we have positive and negative values. We do this in order to show the magnitude of the oscillations relative to the mean, allowing them to be more easily distinguished and for the phase difference to be more conspicuous.

Taking a fast Fourier transform (FFT) of the experimental difference spectrograms in Fig. 2(a) with respect to the probe time-delay axis produces Fig. 4(a). The probe pulse delay increases in 6-fs steps from -294 fs to 5568 fs, which means the FFT frequency resolution is about 0.7 meV. Similarly, from Fig. 2(b) we obtain the theoretical FFT results shown in Fig. 4(b). Quantum beat frequencies are determined by the energetic separation between pairs of beating states in the wave packet. In this panel we indicate the locations of all possible quantum beats from the four initial states. These spectrograms reinforce the strong contribution to the total signal from the $(3d', 5s')$ pair in both core channels. In Fig. 4(b) the amplitude shown at remaining beat frequencies shows the weaker contributions from other pairs of states which are not as evident in Fig. 4(a).

In both theory and experimental panels, taking a line out at the frequency corresponding $(3d', 5s')$, around 0.45 eV, results in Fig. 5. Since the result of the FFT is a complex number, Fig. 5(a) shows the amplitude of the signal and Fig. 5(c) shows the phase of the complex signal, denoted by $\phi_{3d',5s'}$. Notice that in both theory and experiment the phase difference
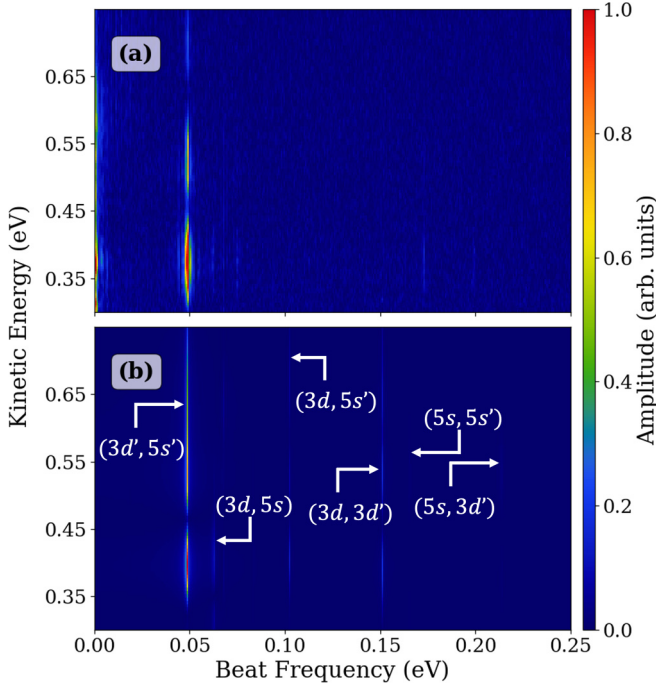
FIG. 4. (a) Amplitude of the fast Fourier transformed difference spectrogram of the experimental data and (b) amplitude of the fast Fourier transformed spectrogram of the theoretical data. They are both normalized to the maximum value of the time-delay mean. In (b) observe the label at the tail of an arrow pointing to the frequency for each one of the pairs of $J = 1$ states.

between the two main peaks is around π radians; we denote this phase difference by $\Delta\phi_{3d',5s'}$. Figure 5(b) shows the individual contributions from $j_c = 1/2$ and $3/2$, showing that there is a single dominant peak on each channel.

IV. THEORY

To describe the process, we need to include the full complexity of the atom in the wave functions. We must describe the atomic states in such a way that they include their components bound to each one of the spin-orbit split ion states and include all possible combinations of angular momentum to account for allowed symmetries. Considering that the two-photon process will mostly be composed of highly excited states, linear combinations of Coulomb functions accurately describe the involved highly excited states. Therefore, we use multichannel quantum defect theory (MQDT) [23–25] to determine the appropriate linear combinations and wave functions for all involved states, except for the neutral argon ground state.

Since both lasers are linearly polarized and parallel, the magnetic quantum number M_J of the total angular momentum is conserved and equal to 0 for all states involved in the process. In the experiment, the spin of the photoelectron is not observed, so we have freedom in choosing the angular momentum coupling scheme for our calculations. We choose the J_{cs} coupling scheme, which couples the total angular momentum of the ion (j_c) with the spin of the electron to form the J_{cs} quantum number, which then couples to the orbital angular
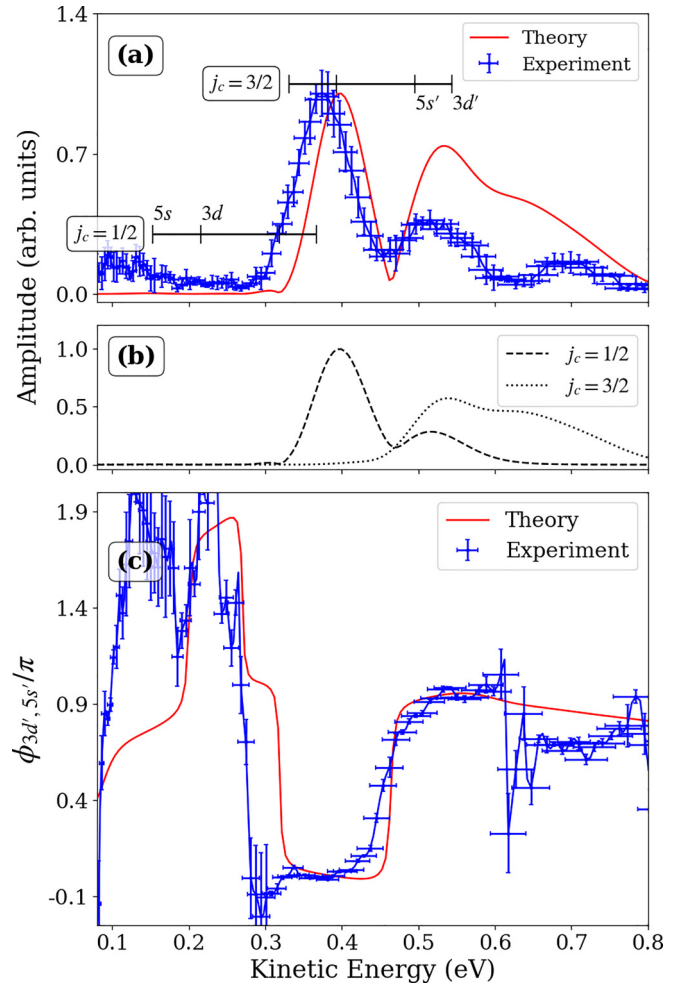

FIG. 5. (a) Fast Fourier transform amplitude of the photoelectron at the $(3d', 5s')$ beat frequency normalized to have unit maximum for the experiment (blue dashed line) and the theory (red solid line). The vertical markers indicate the position of a two-IR-photon ionization from each one of the $J = 1$ states, with respect to each ionic threshold. (b) Amplitude of the individual threshold components for the $(3d', 5s')$ beat. The solid signal of (a) is the coherent sum of these two curves. (c) Phase of the fast Fourier transform of the photoelectron signal for experiment (blue dashed line) and theory (red solid line). Note that the phase makes a jump of nearly π when transitioning from the $j_c = 1/2$ peak to the $j_c = 3/2$ peak.

momentum of the photoelectron to form the total angular momentum J. This simplifies the analysis of the photoelectron signal as it represents an incoherent sum over the J_{cs} values of 0, 1, or 2, constrained by the dipole selection rules. We extend this coupling scheme for all the bound states in our calculations.

We find that the large magnitude of the dipole coupling between the initial $5s$, $3d$, $5s'$, and $3d'$ states and intermediate states makes this process highly nonperturbative. Therefore, we must use a time propagator to describe the dynamics properly. In the following section we describe the MQDT parameters that are necessary to describe the involved symmetries of the atom, as well as the way states at different energies are obtained from these parameters. Next we describe the method used for time propagation.

A. Multichannel quantum-defect theory

To use MQDT, we first have to identify the symmetries involved. From the ground state, the absorption of a single XUV photon can only excite the $J^\pi = 1^o$ symmetry, with five channels for which the MQDT parameters are known [26]. From these states, two symmetries are accessible with one-photon IR probe absorption, $J^\pi = 0^e$, and 2^e with two and six available channels, respectively. For the former, we carry out numerical fits for the energy regions of interest, and for the latter, we use the parameters fitted to experiment in [27].

Finally, following absorption of another IR probe photon causes photoionization to the $J^\pi = 1^o$ and 3° symmetries. In the continuum, the MQDT parameters are known for both symmetries [26,28]. In particular, for $J = 3$, Ref. [28] provides fits for the three outer d electron channels, and we assume that the remaining three g channels have negligible quantum defects. These make up one part of the continuum, 11 channels in total. Similarly to what was observed in [22], taking into consideration the Raman transitions is fundamental for describing the full dynamics of the atom. From the intermediate $J^\pi = 2^e$ states, the emission of a single IR probe photon is nearly resonant with $J^\pi = 3^o$ states, which would then require us to add $J^\pi = 4^e$ intermediate states and an additional $J^\pi = 5^o$ symmetry to the continuum, which adds six more channels. Given the large angular momentum of the channels for the latter two symmetries, we assume a zero quantum defect.

Numerical experiments have shown that excluding these additional symmetries has an impact on the spectrograms. It alters the relative photoionization of each threshold, making $j_c = 3/2$ more dominant. This can be attributed to the coupling between the intermediate unprimed states and these deep $J = 3$ states, reducing photoionization. This effects highlight the importance of the physics incorporated by including these states in the calculation. Furthermore, symmetry considerations indicate that if the observed photoionization were a result of absorbing two IR probe photons, the degree of the anisotropy coefficients found in the photoelectron angular distribution would be 6. However, preliminary observations of the experimental results seem to suggest that they could be noninsignificant to order 8. This certainly agrees with the possible pathways allowed by including these intermediate $J = 3$ states, but this would imply the existence of a tenth degree coefficient, which seems to be small enough to be indistinguishable from the noise. We leave the precise measurement of angle-resolved effects and the analysis of partial cross sections as topics for future investigations.

In summary, to account for all the dynamics of the processes we consider deep bound states, energies around 13.86 and 14.26 eV above the ground state, of angular momentum and parities 1° and 3° with five and six channels, respectively. The intermediate states will have total angular momentum and parities 0^e, 2^e, and 4^e, with two, six, and six channels. Finally, the continuum states will have total angular momentum and parities 1°, 3°, and 5° with five, six, and six channels. This states were chosen in order to fulfill the dipole selection rules imposed by the alignment of the two lasers. All the states will have $M_J = 0$, which is conserved throughout.

For the ionization channels [25], we use the J_{cs} angular momentum coupling scheme, and for the radial wave function, we use the MQDT functions beyond the reaction zone. They are extended to the whole radial domain by using the Seaton-Burgess regularization [29].

In the formulas below, i denotes the ionization channel index and functions Φ_i encompass the wave functions of the core degrees of freedom and the coupled angular momentum states in the ionization channel coupling scheme. The functions f_i and g_i are the regular and irregular Coulomb functions evaluated at the channel kinetic energy, measured from the threshold energy I_i, and the angular momentum corresponding to the outermost electron. Some essential auxiliary functions [25] include the incoming or outgoing wave solutions $f^\pm \equiv (-g \pm if)/\sqrt{2}$ and the energy normalized Whittaker function $W = \cos[\pi(\nu - \ell)]f + \sin[\pi(\nu - \ell)]g$, where ν is defined in terms of the total energy E for each ionization channel through $E = I_i - 1/2\nu_i^2$, in atomic units. In the MQDT eigenchannel parametrization, α denotes the eigenchannel index, and the matrix $U_{i\alpha}$ is the frame transformation matrix that changes the basis between the inner eigenchannels and the ionization channels. Here the eigenchannels are very close to the LS-coupled channels, so this matrix is a small modification of the analytically known angular momentum recoupling matrix. (For more details, see [24–26].) Finally, a channel is designated as closed if the electron's asymptotic kinetic energy is negative; a channel is open if the electron's kinetic energy is positive at infinity.

Below both thresholds, the purely bound states exist only for discrete energies and are given by

$$\left| \Psi_n^J \right\rangle = \mathcal{A} r^{-1} \sum_\alpha A_{n,\alpha}^J \sum_i \Phi_i [f_i(r) U_{i\alpha} \cos(\pi\mu_\alpha) - g_i(r) U_{i\alpha} \sin(\pi\mu_\alpha)]. \tag{1}$$

Here $\mathcal{A}$ denotes the antisymmetrization operator which has no significant effect since the electrons are in different regions of space. We determine the energy of the state and the value of the coefficients A by solving a determinantal equation that requires the wave function to vanish as $r \to \infty$ [25].

Between thresholds, there is an independent solution for any energy and every available open channel. These solutions have a rich resonance structure that stems from the necessity of imposing the appropriate boundary conditions in the closed channels. For an incoming-wave boundary condition state producing outgoing waves only in open ionization channel i', the wave function has the form

$$\psi_{i'}^{(-)} = \mathcal{A} \sum_{i \in o} \frac{1}{r} \Phi_i(\omega) [f_i^+(r)\delta_{ii'} - f_i^-(r) S_{ii'}^{\dagger\,\mathrm{phys}}]$$
$$+ \sum_{i \in c} \frac{1}{r} \Phi_i(\omega) W_i(r, \nu_i, l_i) Z_{ii'}. \tag{2}$$

We have introduced the so-called physical S matrix that describes scattering among the open channels. This matrix and the density of states in the closed channels, the Z coefficients, are obtained by imposing vanishing boundary conditions on the closed channels. This is explained in more detail in [25].

Finally, when the energy is above both thresholds, there is an incoming-wave boundary condition state solution for every

open channel

$$\psi_{i'}^{(-)} = \mathcal{A} \sum_i \frac{1}{r} \Phi_i(\omega)[f_i^+(r)\delta_{ii'} - f_i^-(r)S_{ii'}^\dagger]. \quad (3)$$

B. Time propagation

To perform the time integration, we construct a constrained Hilbert space composed of seven deep bound states that are reachable by the ninth harmonic of the driver laser from the ground state. We include the four ($5s$, $3d$, $5s'$, and $3d'$) $J^\pi = 1^o$ states, which are coupled to the ground state with the dipole elements obtained from their experimentally measured lifetimes [19], and three $J^\pi = 3^o$ states, populated by Raman transition with the IR probe. In addition, we include 54 $J^\pi = 2^e$, 17 $J^\pi = 0^e$, and 26 $J^\pi = 4^e$ intermediate states within reach of single-photon absorption. For these three symmetries, we include 36 states per open channel for states in between thresholds. In this energy region, there is a solution for every energy, but we include only the resonant energies, given that these will have the largest excitation probability. We refer to [22] for the dynamics associated with these states when interacting with the probe. Finally, we include 300 continuum states per channel sampled uniformly in the energy range between 0.5 and 1.5 eV above the highest threshold.

We assume a Gaussian laser pulse with time dependence

$$V(t) = \mathcal{E}_0 e^{-[(t-t_0)/\gamma]^2} \cos(\omega t)\hat{\epsilon} \cdot \vec{r} \equiv F(t, t_0)\hat{\epsilon} \cdot \vec{r} \quad (4)$$

as the time-dependent perturbation, with time propagation handled using the split-operator formula as proposed in [30]. In summary, every time step is divided into three sections: a propagation for half a step of the unperturbed Hamiltonian, which is diagonal in the current basis, a propagation for a complete time step through the perturbation, and then another propagation for half a step through the unperturbed Hamiltonian. The second propagation uses the propagator matrix

$$T_{n,n'}(t, t+\delta t) = \sum_k R_{nk} \exp[-i\mathcal{F}(t, t_0)\lambda_k]R_{kn'}^T, \quad (5)$$

where $\mathcal{F}(t, t_0) = \int_t^{t+\delta t} dt' F(t', t_0)$ and R and λ_k are the eigenvector matrix and eigenvalues of the dipole operator $\hat{\epsilon} \cdot \vec{r}$, respectively, which, since this problem only deals with linearly polarized lasers, reduces to the z operator throughout.

Since we aim to propagate the wave function for a wide range of time delays, it is imperative to implement a fast way to perform many calculations and achieve an acceptable resolution in a manageable timescale. To achieve this, we exploit the linearity of Schrödinger's equation and divide the propagation into two parts.

First, the initial propagation acts on the wave function initialized as the atomic ground state. It evolves through the pump pulse, and the final amplitudes are stored in memory. Since the seven deep bound states are nearly resonant, these are the ones that obtain the highest amplitude in the propagation. Second, we perform a propagation over the probe pulse at zero time delay, initializing the wave function on each of the seven deep bound states and storing the final coefficients in memory.

We compute the final amplitudes for a time delay where the pulses do not overlap. This involves making a linear combination of the states obtained in the propagation of each one of the bound states, phase shifted by the time delay using the corresponding unperturbed energy and of course weighted by the amplitudes obtained with the propagation over the pump.

As a final measure, to ensure an adequate comparison with the experiment, the calculation uses the experimental value for the energies from [19] of the seven deep bound states. This approximation is justified, given that the energies predicted by the MQDT model are, on average, separated from their experimental value by only 4.79 meV. We also convolve the obtained theoretical signal over a Gaussian with energy-dependent width to account for the reconstruction of the spectrograms from the VMI.

V. DISCUSSION

We perform simulations using the following parameters that closely follow the experimental conditions: the pump consisting of all odd harmonics of a 1.59-eV driver (up to the ninth), with 12-fs duration and peak intensity of 1 MW/cm², while the 1-eV IR probe intensity is set to 1 TW/cm², with 65.5-fs duration. Our simulations show good agreement with the experimental observations. First, a comparison of Figs. 2(a) and 2(b) qualitatively shows the agreement between the two signals in terms of the relative strength of the beats, as well as the frequency content and the relative phase across the entire energy range observed. One aspect where we observe a significant difference is the contrast in the oscillations for ionization with respect to the $j_c = 3/2$ threshold. This is confirmed quantitatively by observing the line outs in Fig. 3(a); the theoretical model accurately captures the width of the features as well as the relative strength between the two peaks. With the help of Fig. 3(b) we can identify that indeed the two dominant components of the observed signal correspond to photoionization of the primed states with respect to both ionic thresholds. Also, we notice that there is a contribution coming from the unprimed states and that there is an overlap of unprimed ionization to the $j_c = 3/2$ threshold and primed ionization to the $j_c = 1/2$ threshold.

A more quantitative analysis of the frequency content, applying the discrete Fourier transform to the data, corroborates that indeed the main signal observed experimentally is also dominant in the theory even if in the theoretical signal more beat frequencies are distinguishable [see Figs. 4(a) and 4(b)]. Although in principle there are 21 possible combinations of beats, including all $J = 1$ and 3 pairs, we observe that in theory and experiment the dominant frequency is the $(3d', 5s')$ beat, even if theoretically there is some additional structure owing to the non-negligible amplitude in the $3d$-$3d'$ beat.

The preceding observations can be explained by noticing that the ninth harmonic is nearly resonant with the energy of the $3d'$ state and that the observed bandwidth of the harmonic is wide enough to excite the $5s'$ state. On top of the fact that the $3d'$ state has nearly resonant excitation, the $3d'$ state also has the largest dipole coupling to the ground state, increasing the likelihood of excitation.

The model can also replicate the phase difference between the two ionization peaks [see Fig. 5(c)]. Both experiment and theory show a phase difference close to π between the energies that correspond to ionization to each one of the atomic

thresholds. The existence of this phase difference is tied to the structure of the dipole elements coupling the intermediate states to the $J = 1$ and 3 states and to the open continuum, which in turn is expressible in terms of fundamental atomic quantities, such as the eigenphase shifts. Also, notice that the model captures the dependence of the phase of this beat on energy remarkably well.

A way to determine the source of this phase difference is to analyze the process in perturbation theory. For simplicity, we will only consider the two-photon process. To determine this phase, we need to determine the amplitude of the $(3d', 5s')$ beat in the photoionization amplitude for each ion channel; then we obtain the amplitude at the peak energy in the continuum. The phase we are trying to explain equals the argument of the complex number given by the ratio between these two amplitudes. We are interested in the phase difference between the peaks of the signals; therefore, we evaluate these amplitudes at the average energy of the $3d'$ and $5s'$ states plus the energy of two photons at the central frequency of the pulse. The explicit expression for the phase difference is

$$\phi_{3d',5s'} = \arg \left(\frac{\sum_{i=2,3,5} Z_{3d',i}^1(E) Z_{5s',i}^{1*}(E) + \sum_{i=1,2,4,5} Z_{3d',i}^3(E) Z_{5s',i}^{3*}(E)}{\sum_{i=1,4} Z_{3d',i}^1(E) Z_{5s',i}^{1*}(E) + \sum_{i=3,6} Z_{3d',i}^3(E) Z_{5s',i}^{3*}(E)} \right) \Bigg|_{E=(E_{3d'}+E_{5s'})/2+2\omega} , \tag{6}$$

with the details of its derivation and the expression for the Z terms given in Appendix B. It suffices to say that the superscripts on the Z quantities refer to the two different J channels and the subscript i (over which we sum incoherently) refers to the independent channels. Starting from the $3d'$ and $5s'$ pair, the numerator captures the amplitude for ionization to the $j_c = 3/2$ threshold, while the denominator represents the amplitude for ionization to the $j_c = 1/2$ threshold.

Even though the parameters that describe the experiment go well beyond perturbation theory, we notice that the phase difference persists as the intensity of the laser is increased, suggesting that this effect is indeed tied to the structure of the dipoles and that it depends on fundamental quantities of the atom that vary slowly with energy and are thus not very sensitive to shifts in the spectrum. Perturbation theory predicts that the phase difference between the oscillations at the same frequency between the two ionization thresholds should be independent of intensity, outside of the effects coming from Stark shifts not considered in perturbation theory. It also predicts that the phase is independent of the initial amplitude of the states, so it is independent of the pump.

The numerical simulations certainly agree far beyond the perturbative regime, suggesting that the reasoning described above explains the main mechanism behind the phase. Of course, the perturbative prediction for the phase difference does not exactly coincide with the observed value given that it ignores important effects such as the ponderomotive shift and the Stark effect. Nonetheless, refer to Fig. 6 and note that there are large regions of the parameter space for which the phase is near π, suggesting that due to the Stark shifts certain states could be driven into resonance and shift this to accommodate such a phase difference value for the present parameters.

This effect is prevalent. We found this phase difference in the aforementioned cases where a different energy difference acts as the dominant beat. Remarkably, we found a similar shift in the case of single-photon photoionization, where the probe frequency is doubled.

The fact that we observed this in the single-photon case was particularly illustrative as we can make some approximations that allows us to derive a more explicit expression for the phase difference. Suppose we were only interested in the single $J^\pi = 0^+$ symmetry of the continuum. This is the simplest case as this symmetry is composed of just one pair of channels, one on each ionic state. The final expression is given by

$$\phi_{3d'5s'} = _\pi \arctan(\alpha_0 |S_{12}|), \tag{7}$$

where the factor α_0 is a real factor involving the difference between eigenquantum defects [25] and mixing angles of the continuum channels. We show the derivation of this formula in Appendix A and give an explicit expression for the leading coefficient. The S matrix involved in the formula is the short-range matrix describing the short-range inelastic electron-ion scattering (see [25]).
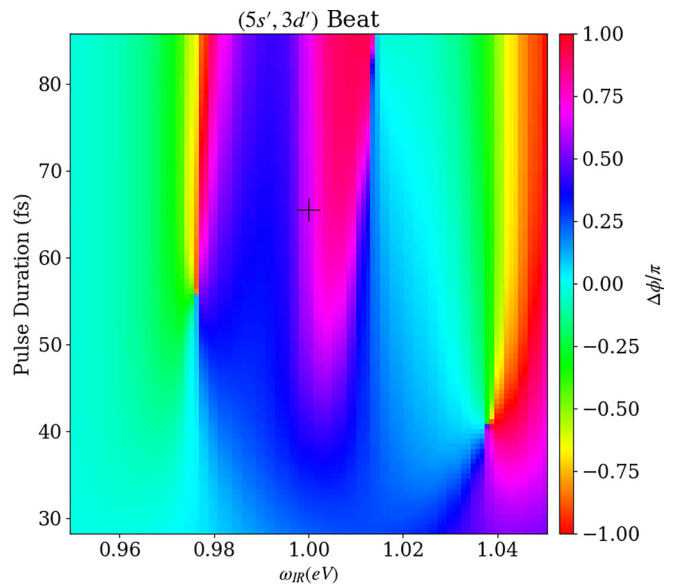

FIG. 6. Obtained phase difference between the two peaks, for the $(5s', 3d')$ states, predicted from perturbation theory as a function of laser duration, which is the full width at half maximum of the intensity of the probe laser and the probe frequency. The strongest dependence comes from the variation on frequency, due to the complicated interplay of resonances. Noticeable is a large plateau around the values near π, which shows evidence that the obtained phase from the time propagation comes from the structure of the dipoles. The plus sign marks the point in the graph of the parameters used in the simulation.

Then each total J partial wave will have a different phase value which then combines to give the one observed in the spectrogram. In this case the alignment of the laser changes and different M_J values are involved and the actual value of the phase difference might change, since the intermediate and final states involved have changed.

Even though we show this only for the single-photon case, it is important to highlight that the structure for the two-photon case is the same and that since the dipole elements between bound states are purely real, the only source for a phase in the final signal comes necessarily from the difference of these eigenphases. Extracting a phase expression beyond perturbation theory is left for future investigation.

Although the phase difference could be explained by perturbation theory, the multiple peaks in the beat amplitude most definitely are not [refer to the structure of the signal in Figs. 5(a) and 5(b)]. The perturbative approach predicts that independent of the intensity of the probe, the profile of the beat amplitude should have only two peaks, one corresponding to each threshold, with the same width. In contrast, we find that the signals show multiple peaks of varied widths. The theory shows a dominant sharp peak with a spread second peak at higher energies. The experiment shows three peaks.

We observe that if the probe intensity or duration changes, multiple peaks in the beat amplitude emerge. This is the consequence of more intermediate energies sustaining interfering pathways. The fact that this depends on the intensity and duration of the laser suggests that it is a consequence of the energy shift in the intermediate states.

Given the large number of states in the propagation and the fact that the energy shift depends on both intensity and frequency, there is no clear method to determine exactly which ones are responsible for the additional peaks. Nonetheless, theoretically, it was found that the amplitude of the beats on each one of the thresholds has two peaks and that the higher peak in the $j_c = 1/2$ channel overlaps with the lower peak of the $j_c = 3/2$ channel [see Fig. 5(b)] and that in the latter the two peaks are overlapping. This, accompanied by the strong dependence on probe duration and intensity, suggests that there are two dominant interfering pathways generating the multipeaked structure for the oscillations at this frequency.

We are able to find a set of parameters that gives rise to the observed peak at around 0.7 eV. This required changing the probe intensity to 2.5 TW/cm^2 and the frequency to 0.972 eV and it induced the $3d$-$3d'$ beat to become more predominant. Performing a partial-wave analysis, it was found that this peak is predominantly composed of $J = 3$ and 5, indicating that the signal comes from the two-photon ionization of the $J = 3$ states, which are excited by a two-photon Raman transition from the $J = 1$ states. The fact that the structure of these peaks depends so strongly on the probe provides more evidence that their existence is tied to the Raman process and makes it very challenging to find a unique set of parameters that captures all features simultaneously. Since the origin of this signal is the fourth-order process it is weak enough not to be observable in the averaged signal over time delay, which is completely dominated by the two-photon signal with symmetry between $J = 1$ and $J = 3$.

All the characteristics observed in the spectrogram of course depend on the pump frequency and we have found that
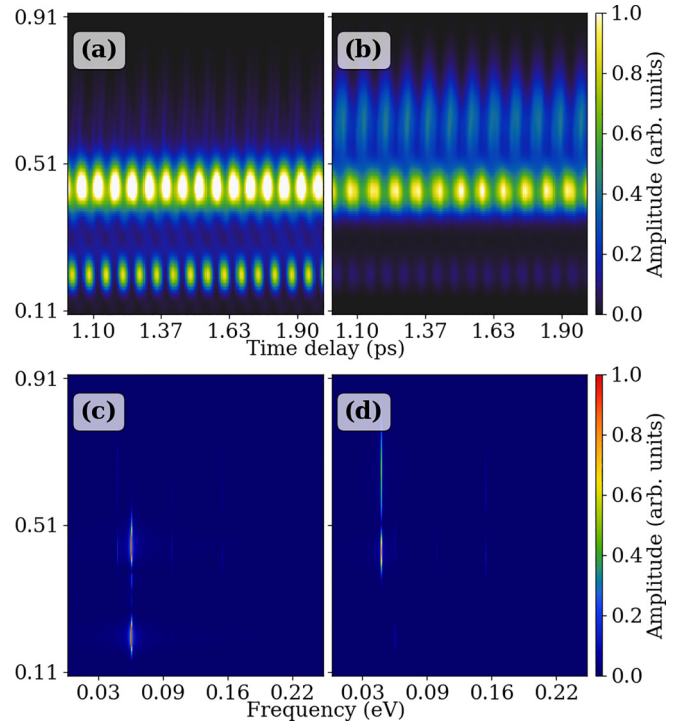

FIG. 7. Spectrograms for two different sets of harmonic frequency. (a) Time-delay spectrogram with harmonic frequency tuned to excite the unprimed states. (b) Time-delay spectrogram with harmonic frequency tuned to excite the primed states. (c) Fast Fourier transform of the spectrogram with the unprimed tuned harmonic. (d) Fast Fourier transform of the spectrogram with the primed tuned harmonic.

manipulating it allows us to make different pairs become the most predominant beat. Making it nearly resonant with the $3d$ state makes the $3d$-$5s$ frequency the most dominant, as in Fig. 7. Similarly, setting the driver frequency so that the ninth harmonic matches the average of the four states makes the $3d$-$3d'$ beat the dominant one since these are the states that couple the strongest with the ground state.

The dependence on the probe parameters comes from variability of the intermediate states as the intensity and frequency of the probe are changed. For example, see Fig. 8(a), which shows the amplitudes obtained for each one of the thresholds. In this case, we see that for a fixed frequency of 1.029 eV the yield to each threshold increases at a different rate. In Fig. 8(b) observe that the phase is not very sensitive to the changing intensity, just as perturbation theory in Appendix B suggests. Finally, in Fig. 8(c) we can observe the obtained spectrograms that qualitatively show the shift in the peak ionization on each threshold induced by the shifts of the intermediate states.

Similarly, in Fig. 9(a) we show the case with a probe intensity of 1 TWcm^{-2} and a probe frequency changing from 0.95 to 1.05 eV. A frequency increase results in a considerable change in the ratio between the time-delay average of ionization on each threshold. In Fig. 9(b) observe that the phase is more sensitive to a change in frequency, as the expression in Appendix B can suggest. Qualitatively, one can observe in Fig. 9(c) the shift in the dominant threshold and how the kinetic energy of the obtained electrons increases with increasing probe frequency.
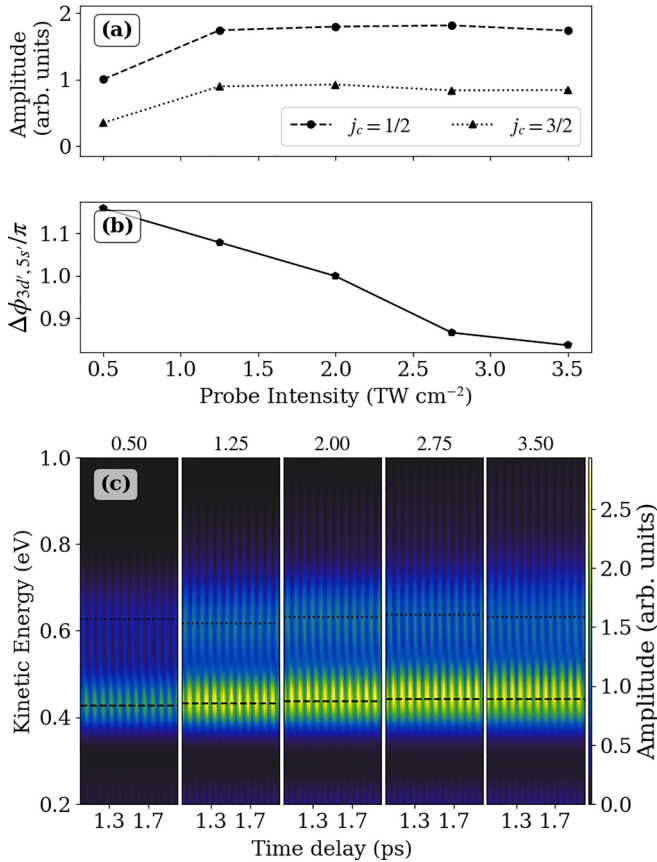
FIG. 8. Intensity dependence of the estimated yield of electrons leaving the ionic core in each of the spin-orbit split states. (a) Amplitudes of the two largest peaks of the time-delay average of the photoionization probability amplitude. (b) Phase difference between $(3d', 5s')$ beat peaks. (c) Spectrogram for each probe intensity plotted in (a), with a horizontal line at which the mean amplitude was obtained for each threshold with dashed lines for $j_c = 1/2$ and dotted lines for $j_c = 3/2$.
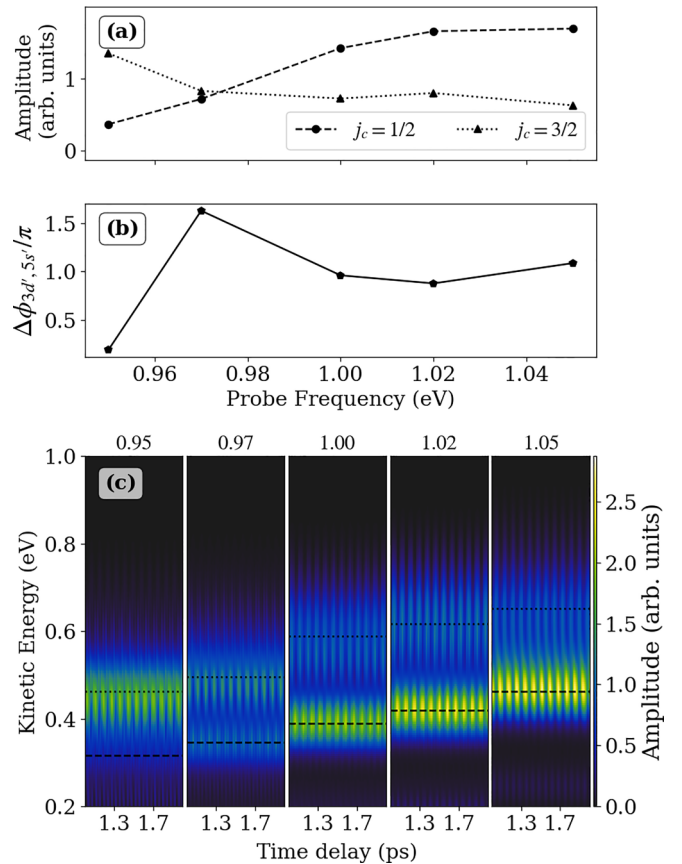

FIG. 9. Frequency dependence of the estimated yield of electrons leaving the ionic core in each of the spin-orbit split states. (a) Amplitude of the dominant peaks on the time-delay average of the photoionization probability. (b) Phase difference between $(3d', 5s')$ beat peaks. (c) Spectrogram for each probe frequency plotted in (a), with a horizontal line at which the mean amplitude was obtained for each threshold with dashed lines for $j_c = 1/2$ and dotted lines for $j_c = 3/2$.

VI. CONCLUSION

Our experimental study highlights several interesting aspects of two-color ionization in the spin-orbit split continuum. The extended theoretical approach introduced here employs MQDT to describe pump-probe spectroscopy experiments. We accurately described the energy distribution of photoelectrons from the argon atom, capturing the dynamics of quantum beat signals as the delay between the pump and the probe is changed. Theory results replicated the frequency content found in the experiment that, even if many pairs of states can interfere, only one pair of states dominates. Our model also captured the variation of the phase of quantum beats on the continuum channel in which the photoelectrons emerge. The remarkable agreement between experiment and theory highlights the importance of accounting for the full structure of the involved bound states, which we achieved by employing the MQDT ideas.

Exploration of the dependence of the observed phase with the system parameters showed that it depends on the off-diagonal elements of the close-range S matrix. To capture this in its simplest form, we explicitly showed the

dependence of phase on these parameters in the single-photon photoionization case. Therefore, by measuring these phases we learned about the electronic interactions in the close range. The formulation of a more general form for this phase outside of perturbation theory is an interesting topic for future research.

Since our theoretical method utilizes a full-time propagation of Schrödinger's equation, it was possible to explore the dependence on different light field parameters. It was found that both the relative amplitude depends considerably on the probe parameters, but the phase between the peaks in the oscillating signals does not have a considerable variation with the intensity and frequency of the probe. Noteworthy is the fact that by varying the frequency of the probe it was possible to change the dominant ionic state from $j_c = 1/2$ to $j_c = 3/2$. It was also possible to explore different values for the harmonic frequency of the pump, showing that by tuning this frequency it was possible to change the value of the dominant beat frequency of the signal.

Our work opens the door for the exploration of different systems of interest since what is required for its

application are the MQDT parameters for the involved symmetries, information that is available with high accuracy for many atoms. Of interest is the neon atom for which recent work [3,31] has shown an interesting dependence of the photoelectron angular distribution on the probe intensity and frequency. Preliminary calculations have shown that our approach can replicate some of the observed results in neon. We leave a detailed study of angular distributions for future investigation.

APPENDIX A: SINGLE-PHOTON CASE IN A TWO-CHANNEL CONTINUUM

1. Phase in terms of eigenphase shift

To illustrate the source of the observed phase from fundamental atomic quantities, we present a simplified model for the process that considers only a single symmetry for the continuum with two channels (as in the case of the $J^\pi = 0^+$ symmetry). Each one of the channels has a different ion state; therefore, we are interested in the phase difference between oscillating probabilities for each channel. Let the bound states that make up the initial wave packet be denoted by $\{\psi_n\}_1^N$.

Now, to determine the wave function in the continuum we will do so in a more explicit way in order to track the source of the phase. Instead of directly calculating the dipole elements of the incoming-wave boundary condition states, we compute the dipoles of standing-wave states and then make a linear combination of the experimentally relevant states [32,33]. In the two-channel case, we will have two independent standing-wave eigenchannel solutions, indexed by ρ.

These states are of the type stressed by Fano [24] and by Lee and Lu [26], which are distinguished by the collision eigenphase shift $\pi\tau_\rho$ and are real. For atomic energy E, above both ionization thresholds, the functional form of this state is

$$\psi_\rho(E) = \mathcal{A}\left(\frac{\Phi_1}{r}[f_1(r)\cos\pi\tau_\rho - g_1(r)\sin\pi\tau_\rho] + \frac{\Phi_2}{r}[f_2(r)\cos\pi\tau_\rho - g_2(r)\sin\pi\tau_\rho]\right) \tag{A1}$$

and the experimentally relevant incoming-wave boundary condition state, which contains only outgoing waves in channel j, is given by the complex superposition

$$\psi_j^- = \sum_\rho \psi_\rho T_{j\rho} \exp[-i(\pi\tau_\rho + \eta_j)], \tag{A2}$$

where η_j is the long-range phase shift of a long-range attractive Coulomb potential and $T_{j\rho}$ is some unitary matrix. In our two-channel case above the two thresholds, we take for this matrix to be orthogonal and parametrized by a single mixing angle

$$T_{j\rho} = \begin{pmatrix} \cos\theta & -\sin\theta \\ \sin\theta & \cos\theta \end{pmatrix}. \tag{A3}$$

The initial wave packet, formed by the pump, is given by

$$\psi(t) = \sum_{n=1}^N A_n(t)\exp(-iE_n t)\psi_n + \int dE\, A_{E,1}(t)\exp(-iEt)\psi_1^-(E) + \int dE\, A_{E,2}(t)\exp(-iEt)\psi_2^-(E), \tag{A4}$$

where the sum is over the bound states and we integrate over the continuum energies above both thresholds and sum over the two distinguishable channels. In the following calculation, we determine the amplitude of the continuum states long after the probe pulse has passed.

As in the main text, we will use the perturbation in Eq. (4). We will assume that at time $t = 0$, the amplitudes in the continuum are zero, while the bound wave packet has nonzero amplitudes, and that the laser has a negligible amplitude. Using time-dependent perturbation theory, we find that for these long times ($t = \infty$) the amplitudes in the continuum under the rotating-wave approximation are

$$A_{E,j}(\infty) = \frac{-i}{2}\sum_n A_n(0)\tilde{F}(E_n + \omega - E, t_0)\langle\psi_j^-|\hat{\epsilon}\cdot\vec{r}|\psi_n\rangle, \tag{A5}$$

where the function $\tilde{F}(\omega, t_0) = \int_{-\infty}^\infty dt\, F(t, t_0)e^{-i\omega t}$. We can explicitly extract the complex component of this amplitude by writing the dipole element in terms of the dipoles with the standing-wave states

$$A_{E,j}(\infty) = \frac{-i}{2}\sum_n A_n(0)\tilde{F}(E_n + \omega - E, t_0)\sum_\rho D_{\rho n}T_{j\rho}\exp[i(\eta_j + \pi\tau_\rho)], \tag{A6}$$

where we define the real dipole elements $D_{\rho n} = \langle \psi_\rho | \hat{\epsilon} \cdot \vec{r} | \psi_n \rangle$. Inserting the explicit expression for the Gaussian pulse and the matrix elements of the T matrix, the expression for the probability is

$$|A_{E,j}(\infty)|^2 = \frac{\mathcal{E}_0^2 \gamma^2 \pi}{8} \sum_{n,n'=1}^N A_n A_{n'}^* \mathcal{P}(E, E_n, E_{n'}) \exp[i(E_n - E_{n'})t_0] \sum_{\rho \rho'} D_{\rho n} D_{\rho' n'} T_{j\rho} T_{j\rho'} e^{i\pi(\tau_\rho - \tau_{\rho'})}, \quad (A7)$$

with $\mathcal{P}(E, E_n, E_{n'}) = \exp\{-\frac{\gamma^2}{8}(E_n - E_{n'})^2 - \frac{\gamma^2}{2}[E - \omega - (E_n + E_{n'})/2]^2\}$. In this sum, n and n' are indices summing over the bound states and hold no relation to the notation in the main text.

In this two-channel case, the probability is given by the sum of four terms, which may be factorized into two. Then the probability for each channel is given by

$$|A_{E,1}(\infty)|^2 = \frac{\mathcal{E}_0^2 \gamma^2 \pi}{8} \sum_{n,n'=1}^N A_n A_{n'}^* \mathcal{P}(E, E_n, E_{n'})(D_{1n}\cos\theta - D_{2n}\sin\theta e^{i\pi(\tau_2-\tau_1)})(D_{1n'}\cos\theta - D_{2n'}\cos\theta e^{i\pi(\tau_1-\tau_2)})e^{i(E_n-E_{n'})t_0} \quad (A8)$$

and

$$|A_{E,2}(\infty)|^2 = \frac{\mathcal{E}_0^2 \gamma^2 \pi}{8} \sum_{n,n'=1}^N A_n A_{n'}^* \mathcal{P}(E, E_n, E_{n'})(D_{2n}\cos\theta + D_{1n}\sin\theta e^{i\pi(\tau_2-\tau_1)})(D_{2n'}\cos\theta + D_{1n'}\cos\theta e^{i\pi(\tau_1-\tau_2)})e^{i(E_n-E_{n'})t_0}. \quad (A9)$$

For the oscillation at frequency $E_n - E_{n'}$, the phase is given by the sum of the phases of the bracketed terms. Since the experiment cannot determine absolute phases, what is measured is the phase difference between the two continuum channels at the energy where the amplitude is maximum, $\mathcal{P}(E, E_n, E_{n'}) = 1$. This is given by

$$\phi_{nn'} =_\pi \arctan\left(\frac{a_0 \sin\Delta \sin 2\theta}{a_1 + a_2\cos 4\theta + a_3\cos 2\theta \sin^2 2\theta + a_4\cos\Delta \sin 4\theta}\right) := \arctan(\alpha_0|S_{12}|),$$

$$a_0 = 4(D_{2n}D_{1n'} - D_{1n}D_{2n'})(D_{1n}D_{1n'} + D_{2n}D_{2n'}),$$

$$a_1 = (D_{2n}^2 - D_{1n}^2)(D_{2n'}^2 - D_{1n'}^2) - 6D_{1n}D_{1n'}D_{2n}D_{2n'},$$

$$a_2 = (D_{2n'}^2 - D_{1n'}^2)(D_{2n}^2 - D_{1n}^2) - 2D_{1n}D_{2n}D_{1n'}D_{2n'},$$

$$a_3 = 4(D_{2n}D_{1n'} + D_{1n}D_{2'})(D_{2n}D_{2n'} - D_{1n}D_{1n'}), \quad (A10)$$

where this equation is valid only modulo π and $\Delta = \pi(\tau_2 - \tau_1)$. Note that these phase differences vanish in the limit that the inelastic electron-ion scattering probability vanishes, which is equal to $|S_{12}|^2 = \sin^2 2\theta \sin^2 \Delta$.

2. Phase in terms of Wigner time delay

This discussion can be translated in terms of time delays, which is of interest to the community given how insightful these delays are when understanding the complex atomic structure and dynamics [16], but the expressions obtained are less transparent. In this case it is more beneficial to work in terms of the dipole transition amplitudes to states that obey the complex incoming-wave boundary condition. Let

$$\langle \psi_j^- | \hat{\epsilon} \cdot \vec{r} | \psi_n \rangle = D_{jn} e^{i\gamma_{jn} + i\eta_j} = \sum_\rho D_{\rho n} T_{j\rho} \exp[i(\eta_j + \pi\tau_\rho)], \quad (A11)$$

where

$$D_{jn} = \sqrt{\sum_{\rho\rho'} D_{\rho n} D_{\rho' n} T_{j\rho} T_{j\rho'}(\cos\pi\tau_\rho \cos\pi\tau_{\rho'} + \sin\pi\tau_\rho \sin\pi\tau_{\rho'})},$$

$$\gamma_{jn} = \arctan\left(\frac{\sum_\rho D_{\rho n} T_{j\rho} \sin\pi\tau_\rho}{\sum_\rho D_{\rho n} T_{j\rho} \cos\pi\tau_\rho}\right). \quad (A12)$$

In term of these phases one can quickly check that

$$\phi_{nn'} = (\gamma_{1n} - \gamma_{2n}) - (\gamma_{1n'} - \gamma_{2n'}), \quad (A13)$$

evaluated at the atomic energy $E = \frac{1}{2}(E_n + E_{n'}) + \omega$.

Nonetheless, in order to relate this to the time delays, we must return to the expression for the probability amplitude and for each term in the sum Taylor expand the energy-dependent phases around $E = E_n + \omega$. The time dependence on the continuum states is

$$A_{E,j}(t \to \infty)\exp(-iEt) = -\frac{i}{2}\sum_n A_n(0)\tilde{F}(E_n + \omega - E, t_0)D_{jn}\exp\{i\eta_j + i\gamma_{jn}^{(0)} + i\gamma_{jn}^{(1)}[E - (E_n + \omega)] - iEt\}, \quad (A14)$$

where the terms $\gamma_{jn}^{(0)}$ indicate evaluating γ_{jn} at energy $E_n + \omega$ and $\gamma_{jn}^{(1)}$ is the first derivative of γ_{jn} evaluated at this same energy.

We interpret this probability amplitude as the sum of terms with different time delays coming from each bound state. The delays correspond to the Wigner time delay $t_{jn} = \gamma_{jn}^{(1)}$ of the photoionization of each one of the bound states. This delay is interpreted as the time difference between an electron ionized from state n into channel j with a photon of frequency ω when the interchannel interactions are included and when they are not. Expanding the probability, we obtain a sum of oscillatory terms

$$|A_{E,j}(\infty)|^2 = \frac{\mathcal{E}_0^2 \gamma^2 \pi}{8} \sum_{n,n'} A_n A_{n'}^* \mathcal{P}(E, E_n, E_{n'}) D_{jn} D_{jn'} \exp\left[i\left(\gamma_{jn}^{(0)} - \gamma_{jn'}^{(0)}\right) - i(t_{jn} E_n - t_{jn'} E_{n'}) + i(t_{jn} - t_{jn'})(E - \omega)\right] e^{i(E_n - E_{n'})t_0}. \tag{A15}$$

Evaluating the amplitude of the $E_n - E_{n'}$ term at the energy of the $\mathcal{P}$ peak, we obtain

$$|A_{E,j}(\infty)|^2\big|_{nn'} = \frac{\mathcal{E}_0^2 \gamma^2 \pi}{8} A_n A_{n'}^* \exp\left(-\frac{\gamma^2}{8}(E_n - E_{n'})^2\right) D_{jn} D_{jn'} \exp\left\{i\left(\gamma_{jn}^{(0)} - \gamma_{jn'}^{(0)}\right) + i(E_n - E_{n'})[t_0 - 1/2(t_{jn} + t_{jn'})]\right\}. \tag{A16}$$

Here the phase added to the beat comes from two different terms. One is the difference of the phase of the complex dipole elements evaluated at the energy of the single-photon absorption. The second term shifts the laser delay t_0 by the average time delay between the two continuum electron waves. This essentially is an adjustment to account for the delay to reach the detector for electrons being ionized from each bound state.

Then the phase difference between the beats is given by

$$\phi_{nn'} = \left(\gamma_{1n}^{(0)} - \gamma_{2n}^{(0)}\right) - \left(\gamma_{1n'}^{(0)} - \gamma_{2n'}^{(0)}\right) - \frac{1}{2}(E_n - E_{n'})(t_{1n} - t_{2n} + t_{1n'} - t_{2n'}), \tag{A17}$$

which is just the first-order Taylor expansion of Eq. (20). However, there is a caveat: The terms related to each one of the bound states are expanded with respect to different energies, which means that this expression is meaningful only if the beat frequency $E_n - E_{n'}$ is not too large compared to the variation of the phases.

The zeroth-order term here mimics the phase difference obtained in the previous derivation in terms of the eigenchannel quantities, although care must be taken as the energy at which incoming-wave boundary condition dipole phases are being evaluated are different.

For the two-channel continuum the expression for the time delays in terms of fundamental quantities is given by

$$t_{1n} = \frac{\sin\Delta(b_0 \sin 2\theta - b_1\dot\theta) + 2\pi[\dot\tau_1 \cos\theta D_{1n}(D_{1n}\cos\theta - D_{2n}\sin\theta\cos\Delta) + \dot\tau_2 \sin\theta D_{2n}(D_{2n}\sin\theta - D_{1n}\cos\theta\cos\Delta)]}{2\left(\cos^2\theta D_{1n}^2 + \sin^2\theta D_{2n}^2 - \cos\Delta\sin 2\theta D_{1n}D_{2n}\right)},$$

$$t_{2n} = \frac{\sin\Delta(-b_0 \sin 2\theta - b_1\dot\theta) + 2\pi[\dot\tau_1 \sin\theta D_{1n}(D_{1n}\sin\theta + D_{2n}\cos\theta\cos\Delta) + \dot\tau_2 \cos\theta D_{2n}(D_{2n}\cos\theta + D_{1n}\sin\theta\cos\Delta)]}{2\left(\sin^2\theta D_{1n}^2 + \cos^2\theta D_{2n}^2 + \cos\Delta\sin 2\theta D_{1n}D_{2n}\right)},$$

$$b_0 = D_{2n}\dot D_{1n} - \dot D_{2n}D_{1n},$$

$$b_1 = 2D_{1n}D_{2n}. \tag{A18}$$

In the limit of constant maximum mixing between channels, $\theta = \pi/4$, the time-delay difference is given by

$$t_{1n} - t_{2n} = \frac{-2\sin\Delta\left(D_{1n}^2 + D_{2n}^2\right)b_0 + \pi b_1 \cos\Delta\left(D_{1n}^2 - D_{2n}^2\right)\dot\Delta}{D_{1n}^4 + D_{2n}^4 - 2\cos 2\Delta D_{1n}^2 D_{2n}^2}. \tag{A19}$$

APPENDIX B: TWO-PHOTON IONIZATION FOR ARGON

Similarly to the single-photon case, the calculation starts from a wave packet formed after the pump laser and we want the amplitudes for times long after the probe pulse has passed. In this case we include all the symmetries of the continuum and consider the dipoles directly to the incoming-wave boundary condition states. The wave packet is composed of seven complex amplitudes A_n for each one of the $J^\pi = 1^o$ and 3° states. We again use Eq. (4) as the time-dependent perturbation and use second-order time dependent perturbation to find the amplitudes in the continuum.

To simplify the calculation, only the two-photon process is treated. The time-dependent unperturbed state is then given by

$$\psi(t) = \sum_n A_n(t)\exp(-iE_n t)\psi_n + \sum_{j=1,\ldots,5} \int dE\, A_{E,j}^{1^o}(t)\exp(-iEt)\psi_j^{1^o-}(E)$$

$$+ \sum_{j=1,\ldots,6} \int dE\, A_{E,j}^{3^o}(t)\exp(-iEt)\psi_j^{3^o-}(E). \tag{B1}$$

As in Appendix A we are interested on the amplitude of the continuum states long after the probe laser has passed. We use the second-order expression for the matrix element of the transition matrix, as presented in [34], to obtain

$$A_{E,i}^{J^\pi}(t \to \infty) = -\sum_n A_n \int d\tau_1 \int d\tau_2 \sum_{J_\xi} \!\!\!\!\!\! \int \!\! dE_\xi \langle \psi_i^{J^\pi}(E)(-1)|V(\tau_1)|\Phi_{E_\xi}\rangle \langle \Phi_{E_\xi}|V(\tau_2)|\psi_n\rangle e^{i(E-E_\xi)\tau_1} e^{i(E_\xi - E_n)\tau_2}$$

$$= -\frac{\mathcal{E}_0^2 \gamma^2 \pi}{8} \sum_n A_n \exp[i(E-E_n)t_0] \exp\left(-\frac{\gamma^2}{8}(E_n + 2\omega - E)^2\right)$$

$$\times \sum_{J_\xi} \!\!\!\!\!\! \int \!\! dE_\xi \langle \psi_i^{J^\pi}(E)(-1)|\hat{\epsilon}\cdot\vec{r}|\Phi_{E_\xi}\rangle \langle \Phi_{E_\xi}|\hat{\epsilon}\cdot\vec{r}|\psi_n\rangle \mathcal{W}\left[\frac{\gamma}{\sqrt{2}}\left(E_\xi - E_n - \omega + \frac{E_n + 2\omega - E}{4}\right)\right], \qquad \text{(B2)}$$

where the function $\mathcal{W}(z) \equiv e^{-z^2}[1 - i\,\mathrm{erfi}(z)]$. The goal of this derivation is to determine the phase difference in the signal between the electrons that leave the core in each of the different spin-orbit split states. To simplify our notation, we define the symbol $Z_{n,i}^{J^\pi}(E)$ as including all the terms involved in the integral sum over intermediate states and their dipole matrix elements. This Z will encompass all the complex phase information to the continuum as well as the complex resonant structure of the intermediate states.

With this, the total probability density for a defined kinetic energy is an incoherent sum of the probabilities over the distinguishable channels,

$$P(\epsilon) = \frac{\mathcal{E}_0^4 \gamma^4 \pi^2}{64} \sum_{n,n'} A_n A_{n'}^* \exp\left(i(E_{n'} - E_n)t_0 - \frac{\gamma^2}{16}(E_n - E_{n'})^2\right) \left\{ \exp\left[-\frac{\gamma^2}{4}\left(E_{3/2} + \epsilon - \frac{E_n + E_{n'}}{2} - 2\omega\right)^2\right]\right.$$

$$\times \left(\sum_{i=2,3,5} Z_{n,i}^1(E_{3/2}+\epsilon)Z_{n',i}^{1*}(E_{3/2}+\epsilon) + \sum_{i=1,2,4,5} Z_{n,i}^3(E_{3/2}+\epsilon)Z_{n',i}^{3*}(E_{3/2}+\epsilon)\right)$$

$$+ \exp\left[-\frac{\gamma^2}{4}\left(E_{1/2} + \epsilon - \frac{E_n + E_{n'}}{2} - 2\omega\right)^2\right]$$

$$\left.\times \left(\sum_{i=1,4} Z_{n,i}^1(E_{1/2}+\epsilon)Z_{n',i}^{1*}(E_{1/2}+\epsilon) + \sum_{i=3,6} Z_{n,i}^3(E_{1/2}+\epsilon)Z_{n',i}^{3*}(E_{1/2}+\epsilon)\right)\right\}. \qquad \text{(B3)}$$

This expression clarifies what defines the amplitude and phase in the beating signal. First, notice that, similarly to what was found in [22] and in the previous derivation for the single-photon case, the interaction term has a Gaussian factor in the difference between the bound-state energies. Second, note that the contributions to each threshold peak at different kinetic energies. To find the phase difference we just take the argument of the ratio between the complex amplitudes of the terms going to each separate threshold at the energy where they peak, $E = (E_n + E_{n'})/2 + 2\omega$:

$$\phi_{n,n'} = \arg\left(\frac{\sum_{i=2,3,5} Z_{n,i}^1(E)Z_{n',i}^{1*}(E) + \sum_{i=1,2,4,5} Z_{n,i}^3(E)Z_{n',i}^{3*}(E)}{\sum_{i=1,4} Z_{n,i}^1(E)Z_{n',i}^{1*}(E) + \sum_{i=3,6} Z_{n,i}^3(E)Z_{n',i}^{3*}(E)}\right)\Bigg|_{E=(E_n+E_{n'})/2+2\omega}. \qquad \text{(B4)}$$

Notably, this phase difference does not depend on the intensity of the probe laser and so it is entirely determined from the central frequency and the bandwidth of the laser. For the values utilized in the spectrogram shown in Fig. 2 and using the intermediate bound states sampled in the sum, we obtain a value of 0.8354π, which is considerably lower than what is observed experimentally. Nevertheless, the phase difference obtained using the perturbative model has a considerable dependence on the frequency of the probe, reaching a value close to π for parameters close to those used experimentally. Even if the perturbative model does not match exactly the phase difference obtained in the experiment, the ac Stark shift due to the probe laser takes the appropriate states in resonance so that the phase obtained agrees reasonably well with that predicted for slightly different parameters.

---

[1] L. D. Noordam and R. R. Jones, Probing Rydberg electron dynamics, J. Mod. Opt. **44**, 2515 (1997).

[2] S. Gilb, E. A. Torres, and S. R. Leone, Mapping of time-dependent electron orbital alignment, J. Phys. B **39**, 4231 (2006).

[3] D. M. Villeneuve, P. Hockett, M. J. J. Vrakking, and H. Niikura, Coherent imaging of an attosecond electron wave packet, Science **356**, 1150 (2017).

[4] R. Forbes, V. Makhija, J. G. Underwood, A. Stolow, I. Wilkinson, P. Hockett, and R. Lausten, Quantum-beat photoelectron-imaging spectroscopy of Xe in the VUV, Phys. Rev. A **97**, 063417 (2018).

[5] P. Zhang, V.-H. Hoang, C. Wang, T. T. Luu, V. Svoboda, A.-T. Le, and H. J. Wörner, Effects of Autoionizing Resonances on Wave-Packet Dynamics Studied by Time-Resolved Photoelectron Spectroscopy, Phys. Rev. Lett. **130**, 153201 (2023).

[6] T. Okino, Y. Furukawa, Y. Nabekawa, S. Miyabe, A. A. Eilanlou, E. J. Takahashi, K. Yamanouchi, and K. Midorikawa, Direct observation of an attosecond electron wave packet in a nitrogen molecule, Sci. Adv. **1**, e1500356 (2015).

[7] A. González-Castrillo, F. Martín, and A. Palacios, Quantum state holography to reconstruct the molecular wave packet using an attosecond XUV–XUV pump-probe technique, Sci. Rep. **10**, 12981 (2020).

[8] T. Remetter, P. Johnsson, J. Mauritsson, K. Varju, Y. Ni, F. Lepine, E. Gustafsson, M. Kling, J. Khan, R. Lopez-Martens, K. J. Schafer, M. J. J. Vrakking, and A. L'Huillier, Attosecond electron wave packet interferometry, Nat. Phys. **2**, 323 (2006).

[9] K. Klünder, P. Johnsson, M. Swoboda, A. L'Huillier, G. Sansone, M. Nisoli, M. J. J. Vrakking, K. J. Schafer, and J. Mauritsson, Reconstruction of attosecond electron wave packets using quantum state holography, Phys. Rev. A **88**, 033404 (2013).

[10] N. Shivaram, H. Timmers, X.-M. Tong, and A. Sandhu, Attosecond-Resolved Evolution of a Laser-Dressed Helium Atom: Interfering Excitation Paths and Quantum Phases, Phys. Rev. Lett. **108**, 193002 (2012).

[11] D. Busto, L. Barreau, M. Isinger, M. Turconi, C. Alexandridi, A. Harth, S. Zhong, R. J. Squibb, D. Kroon, S. Plogmaker, M. Miranda, Á. Jiménez-Galán, L. Argenti, C. L. Arnold, R. Feifel, F. Martín, M. Gisselbrecht, A. L'Huillier, and P. Salières, Time-frequency representation of autoionization dynamics in helium, J. Phys. B **51**, 044002 (2018).

[12] E. P. Månsson, D. Guénot, C. L. Arnold, D. Kroon, S. Kasper, J. M. Dahlström, E. Lindroth, A. S. Kheifets, A. L'Huillier, S. L. Sorensen, and M. Gisselbrecht, Double ionization probed on the attosecond timescale, Nat. Phys. **10**, 207 (2014).

[13] J. Feist, S. Nagele, C. Ticknor, B. I. Schneider, L. A. Collins, and J. Burgdörfer, Attosecond Two-Photon Interferometry for Doubly Excited States of Helium, Phys. Rev. Lett. **107**, 093005 (2011).

[14] S. Pabst and J. M. Dahlström, Eliminating the dipole phase in attosecond pulse characterization using Rydberg wave packets, Phys. Rev. A **94**, 013411 (2016).

[15] J. M. Dahlström, S. Pabst, and E. Lindroth, Pulse analysis by delayed absorption from a coherently excited atom, APL Photon. **4**, 011101 (2019).

[16] I. Jordan, M. Huppert, S. Pabst, A. S. Kheifets, D. Baykusheva, and H. J. Wörner, Spin-orbit delays in photoemission, Phys. Rev. A **95**, 013404 (2017).

[17] M. Turconi, L. Barreau, D. Busto, M. Isinger, C. Alexandridi, A. Harth, R. J. Squibb, D. Kroon, C. L. Arnold, R. Feifel, M. Gisselbrecht, L. Argenti, F. Martín, A. L. 'Huillier, and P. Salières, Spin–orbit-resolved spectral phase measurements around a Fano resonance, J. Phys. B **53**, 184003 (2020).

[18] S. Pabst and R. Santra, Spin–orbit effects in atomic high-harmonic generation, J. Phys. B **47**, 124026 (2014).

[19] A. Kramida, Y. Ralchenko, J. Reader, and NIST ASD Team, NIST Atomic Spectra Database, available at https://physics.nist.gov/asd.

[20] A. Plunkett, N. Harkema, R. R. Lucchese, C. W. McCurdy, and A. Sandhu, Ultrafast Rydberg-state dissociation in oxygen: Identifying the role of multielectron excitations, Phys. Rev. A **99**, 063403 (2019).

[21] G. A. Garcia, L. Nahon, and I. Powis, Two-dimensional charged particle image inversion using a polar basis function expansion, Rev. Sci. Instrum. **75**, 4989 (2004).

[22] A. Plunkett, M. A. Alarcón, J. K. Wood, C. H. Greene, and A. Sandhu, Raman Interferometry between Autoionizing States to Probe Ultrafast Wave-Packet Dynamics with High Spectral Resolution, Phys. Rev. Lett. **128**, 083001 (2022).

[23] M. Seaton, Quantum defect theory, Rep. Prog. Phys. **46**, 167 (1983).

[24] U. Fano, Quantum defect theory of l uncoupling in H_2 as an example of channel-interaction treatment, Phys. Rev. A **2**, 353 (1970).

[25] M. Aymar, C. H. Greene, and E. Luc-Koenig, Multichannel Rydberg spectroscopy of complex atoms, Rev. Mod. Phys. **68**, 1015 (1996).

[26] C. M. Lee and K. T. Lu, Spectroscopy and collision theory. II. The Ar absorption spectrum, Phys. Rev. A **8**, 1241 (1973).

[27] M. Pellarin, J. L. Vialle, M. Carré, J. Lermé, and M. Aymar, Even parity series of argon Rydberg states studied by fast-beam collinear laser spectroscopy, J. Phys. B **21**, 3833 (1988).

[28] J. M. Weber, K. Ueda, D. Klar, J. Kreil, M. W. Ruf, and H. Hotop, Odd Rydberg spectrum of ^{40}Ar(I) : High-resolution laser spectroscopy and multichannel quantum defect analysis of the $J = 2$ and 3 levels, J. Phys. B **32**, 2381 (1999).

[29] A. Burgess and M. J. Seaton, A general formula for the calculation of atomic photo-ionization cross sections, Mon. Not. R. Astron. Soc. **120**, 121 (1960).

[30] M. Tarana and C. H. Greene, Femtosecond transparency in the extreme-ultraviolet region, Phys. Rev. A **85**, 013411 (2012).

[31] S. Patchkovskii, M. J. Vrakking, D. M. Villeneuve, and H. Niikura, Selection of the magnetic quantum number in resonant ionization of neon using an XUV-IR two-color laser field, J. Phys. B **53**, 134002 (2020).

[32] M. D. Lindsay, C.-J. Dai, L.-T. Cai, T. F. Gallagher, F. Robicheaux, and C. Greene, Angular distributions of ejected electrons from autoionizing 3pnd states of magnesium, Phys. Rev. A **46**, 3789 (1992).

[33] C. H. Greene and C. Jungene, Molecular applications of quantum defect theory, Adv. At. Mol. Phys. **21**, 51 (1985).

[34] F. H. M. Faisal, *Theory of Multiphoton Processes* (Springer, New York, 1987).